

Possible signature of distant foreground in the Planck data

V. N. Yershov^{1,2*}, V. V. Orlov^{2,3} and A. A. Raikov²

¹Mullard Space Science Laboratory, University College London, Holbury St.Mary, Dorking, RH5 6NT U.K.

²Main (Pulkovo) Astronomical Observatory of the Russian Academy of Sciences, 65 Pulkovskoe shosse, 196140, St.Petersburg, Russia

³Saint Petersburg State University, 28 Universitetskij prospect Peterhof, 198504, St.Petersburg, Russia

Accepted 2014 September 16. Received 2014 September 15; in original form 2013 December 17

ABSTRACT

By using the Planck map of the cosmic microwave background (CMB) radiation we have checked and confirmed the existence of a correlation between supernova (SN) redshifts, z_{SN} , and CMB temperature fluctuations at the SNe locations, T_{SN} , which we previously reported for the Wilkinson Microwave Anisotropy Probe data. The Pearson correlation coefficient for the Planck data is $r = +0.38 \pm 0.08$ which indicates that the correlation is statistically significant (the signal is about 5σ above the noise level). The correlation becomes even stronger for the type Ia subsample of SNe, $r_{\text{Ia}} = +0.45 \pm 0.09$, whereas for the rest of the SNe it is vanishing. By checking the slopes of the regression lines $T_{\text{SN}}/z_{\text{SN}}$ for Planck’s different frequency bands we have also excluded the possibility of this anomaly being caused by the Sunyaev-Zeldovich effect. The remaining possibility is some, unaccounted for, contribution to the CMB from distant ($z > 0.3$) foreground through either the integrated Sachs-Wolfe effect or thermal emission from intergalactic matter.

Key words: supernovae: general — galaxies: star formation — dust — cosmic background radiation — methods: statistical

1 INTRODUCTION

Previously we reported (Yershov et al. 2012) an anomaly found in the cosmic microwave background (CMB) radiation, that manifested itself as a positive correlation between supernova (SN) redshifts and CMB temperature fluctuations measured by the Wilkinson Microwave Anisotropy Probe (WMAP) at the SN locations. In particular, the WMAP CMB map temperatures corresponding to different SN redshifts revealed an excess of temperatures $+29.9 \pm 4.4 \text{ } [\mu\text{K}]$ for the redshift range $z \sim 0.5$ to 1.0.

When discussing the possible origin of this anomaly, we have excluded the energy-dependent Sunyaev-Zeldovich (SZ) effect (Sunyaev & Zeldovich 1970) by comparing the magnitude of the anomaly in different WMAP frequency bands. The remaining possibilities were the contribution from either dust or the integrated Sachs-Wolfe (ISW) effect (Sachs & Wolfe 1967). For example, a similar band-independent correlation between WMAP temperatures and large-scale structures traced by galaxies was found by Goto et al. (2012) for the Wide-field Infrared Survey Explorer data, which was attributed by the authors to the Sachs-Wolfe effect. This effect alters the energy of CMB photons when these photons traverse gravitational fields of different strengths corresponding to either voids or clumps

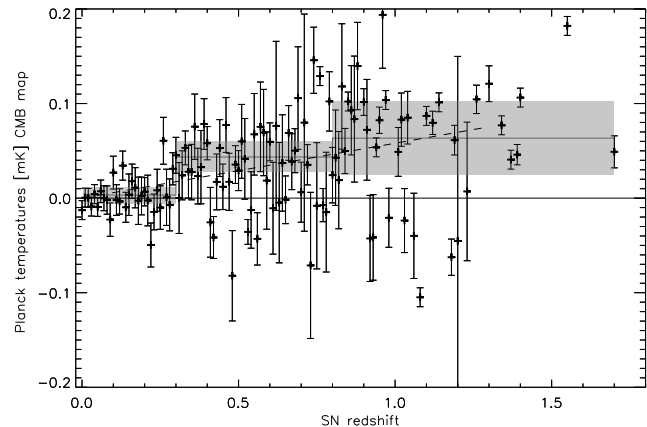


Figure 1. Planck CMB temperatures T_{SN} near the supernovae locations as a function of SN redshift z_{SN} . The dashed line indicates the slope $\xi = +58.0 \pm 9.0 \text{ } [\mu\text{K}]$ of the linear regression $T_{\text{SN}} = \xi z_{\text{SN}}$. The shaded area indicates the $\pm 3\sigma$ tolerances around the \bar{T}_{SN} averaged within three SN redshift intervals: $z < 0.3$, $0.3 < z < 0.8$ and $z > 0.8$.

of matter, the photon energy being increased for clumps and decreased for voids.

In the case of SNe, both effects could be simultaneous because SNe obviously occur in clumps of matter,

* E-mail: v.yershov@ucl.ac.uk

but many of them are also known to be affected by high extinction in their host galaxies, indicating the presence of dust (Di Paola et al. 2002; Vink 2004; Elias-Rosa et al. 2008; Kozlovski et al. 2010; Romero-Canizales et al. 2012; Mattila et al. 2012).

After the release of the ESA’s Planck space telescope data (Planck Collaboration 2014), it was instructive to check the presence of the same anomaly using a higher quality data set obtained by a different instrument for different frequency bands. Here we present the results of such a check for the released Planck CMB map, as well as for its five (of nine) frequency bands.

2 PLANCK CMB DATA AND THE SUPERNOVA REDSHIFTS

For our analysis we have taken the list of supernovae (Bartunov et al. 2007) maintained by the Sternberg Astronomical Institute (Moscow) at <http://www.sai.msu.su/sn/sncat> which contains a large sample of SNe with known redshifts (6365 SNe as for October 2013). The Planck data products were obtained from ESA’s Planck Legacy Archive (Planck Collaboration 2014) at <http://www.sciops.esa.int/pla/aio>, and the software for processing these data was adopted from the comprehensive HEALPIX package developed by Jet Propulsion Laboratory and available at <http://healpix.jpl.nasa.gov> (Gorski et al. 2005).

We have constructed a diagram of the Planck CMB pixel temperatures at the SN locations as a function of SN redshifts. Figure 1 shows this diagram for the Planck CMB map produced by the semi-parametric processing pipeline (SMICA R1.20).

In order to avoid contamination from point sources and from the galactic plane, we have used the Planck confidence map containing pixels with an expected low level of foreground contamination, as well as the Plank High Frequency Instrument’s (HFI) point source and galactic plane masks. Additionally, we have restricted our SN sample to high galactic latitudes $|b| > 40^\circ$ and to the SN redshifts $z_{\text{SN}} > 0.05$. The 1048 SNe with $z < 0.05$ were irrelevant for our study, so the remaining sample used for checking the relationship between the Planck CMB map pixel temperatures and SN redshifts consisted of 3348 SNe. By grouping the Planck CMB pixel temperatures into the SN redshift bins with the bin size of 0.01, we have obtained the diagram shown in Fig. 1.

The average temperature for the selected latitude range can differ from zero by being based on a subset of the Planck data (the zero average corresponds to the whole set of pixels covering the entire celestial sphere). Since we are interested in the possible relationship between the SN redshifts and the CMB temperature fluctuations, we can subtract any constant value from the bin-averaged temperatures. What is important is the slope ξ of the regression line $T_{\text{SN}} = \xi z_{\text{SN}}$ characterising the relationship between the SN redshifts and CMB temperatures. This regression line with $\xi = 58.0 \pm 9.0$ (in μK per redshift unit) is shown in Fig.1 as the dashed line. The temperature zero-level for this diagram was adjusted in such a way that to nullify the average $\overline{T}_{\text{SN}}^{0.05} = +2.7 [\mu\text{K}]$ for the local SNe with $z_{\text{SN}} < 0.05$.

Table 1. Temperatures \overline{T}_{SN} averaged for three large redshift intervals (bins) $0.0 < z_1 < 0.3$, $0.3 < z_2 < 0.8$ and $0.8 < z_3 < 1.7$.

Characteristics	z_1	z_2	z_3
$\overline{T}_{\text{SN}} [\mu\text{K}]$	+3.2	+43.5	+63.4
$\sigma_{\overline{T}_{\text{SN}}} [\mu\text{K}]$	± 2.9	± 5.4	± 12.9
Signal-to-noise ratio $[\sigma]$	1.0	7.9	4.9
Sample size	2741	516	91

Like in the WMAP case, the diagram shown in Fig.1 exhibits a positive anomaly of T_{SN} for high redshifts. The error-bars of T_{SN} in this diagram correspond to the weighted standard errors (SE_w) of the averages $\overline{T}_{\text{SN}}^w$ in each redshift bin calculated as

$$SE_w = \sqrt{\sigma_w^2 \sum_{i=1}^n w_i^2 / (\sum_{i=1}^n w_i)^2},$$

where

$$\sigma_w^2 = \sum_{i=1}^n w_i (T_{\text{SN}}^i - \overline{T}_{\text{SN}}^w)^2 / (\sum_{i=1}^n w_i - 1),$$

$$\overline{T}_{\text{SN}}^w = \sum_{i=1}^n w_i T_{\text{SN}}^i / \sum_{i=1}^n w_i,$$

and n is the number of SNe in the bin. The individual weights w_i of the Planck CMB pixel temperatures T_{SN}^i were obtained by using the variances given for these temperatures in the Plank data tables. The points in Fig.1 corresponding to the cases with a single source in a redshift bin (which are mostly the points with $z_{\text{SN}} > 1.3$) are shown with the error-bars transferred from the Planck variance map for the CMB temperatures T_{SN}^i . The average number of SNe in each redshift bin was 60.8 for $z_{\text{SN}} < 0.5$ and 2.6 for $z_{\text{SN}} \in (0.5, 1.0)$, with the total number of 3348 SNe in the selected latitude range.

Since the number of T_{SN}^i values in each bin is relatively small for high redshifts, we have also produced \overline{T}_{SN} averaged within three much larger redshift intervals, $z_1 < 0.3$, $0.3 < z_2 < 0.8$ and $0.8 < z_3 < 1.7$, whose sizes are roughly proportional to the physical distance intervals. The results of this averaging are presented in Table 1 and in the form of shaded areas in Fig.1 indicating the $\pm 3\sigma$ tolerance intervals for the averages. This three-bin averages highlight the anomaly more clearly, showing that the \overline{T}_{SN} signal exceeds the noise level by about 7σ for z_2 .

The magnitude of this anomaly is higher than the anomaly previously reported for the WMAP data, which can be attributed to the different from WMAP set of frequency bands used in the Planck experiment. Part of this difference might also be due to the lesser averaging effect in the Planck data compared to WMAP because of higher angular resolution of the Planck instruments.

The Pearson correlation coefficient for our binned data is $r = 0.38 \pm 0.08$. The confidence interval here was calculated by bootstrapping the correlation (Efron 1979). This method consists in repeatedly resampling the data many times, each time calculating the correlation coefficient and, finally, getting the standard deviation of the generated in this way distribution of r values. The calculated confidence

interval does not include $r = 0$ at about 4.6σ significance level, which indicates the statistical significance of the correlation. The same bootstrapping method was also used for calculating the tolerance interval (± 9.0 [μK]) corresponding to the slope of the regression line $T_{\text{SN}}/z_{\text{SN}}$ (the dashed line in Fig.1).

The Pearson correlation coefficient calculated for the unbinned SN data is essentially smaller, but so is its bootstrap confidence interval: $r_{\text{unbinned}} = 0.130 \pm 0.016$. This shows that the estimate of the statistical significance of the found correlation does not depend on the degree of data binning/smoothing. Moreover, the calculation of the slope of the regression line for the unbinned data gives the same result as for the case when the data are binned: $\xi_{\text{unbinned}} = 57.1 \pm 7.0$ [μK].

Yet another check ensuring that the seen correlation is not due to a systematic error in our calculations consists in randomising the SN positions on the sky. For this purpose, we have used the same SNe but with their galactic longitudes randomised, while keeping the same declination range ($|b| > 40^\circ$) as for the original SN sample. The $T_{\text{SN}}/z_{\text{SN}}$ diagram for the randomised SN sample (shown in the upper panel of Fig.2) does not reveal any temperature anomalies, the average temperatures for the three selected redshift intervals being $\overline{T}_{\text{SN}_{\text{rand}}}^{z_1} = 4.1 \pm 3.1$ [μK], $\overline{T}_{\text{SN}_{\text{rand}}}^{z_2} = 3.9 \pm 5.1$ [μK], $\overline{T}_{\text{SN}_{\text{rand}}}^{z_3} = -3.1 \pm 12.1$ [μK].

The latter test confirms that the positive anomaly seen in the Planck CMB pixel temperatures is indeed related to the SN locations. Those, in turn, trace the presence of distant ($z > 0.3$) concentrations of matter (distant foreground), which might be behind the origin of the anomaly.

Although the processing scheme used for generating the Planck CMB map was taking into account the local foreground emission from gas and dust belonging to our Galaxy, some fraction of this emission still might be left unaccounted for in the Planck CMB map product. It is for this reason that we have used a subsample of SNe, limiting their coordinates to the region with the galactic latitudes $|b| > 40^\circ$. However, it would be instructive to check to what degree the local foreground, obscures the systematic relationship between T_{SN} and z_{SN} seen for the high-latitude SNe. For this purpose we have performed the correlation analysis of the Planck CMB map for the sample of 5318 SNe covering the whole galactic latitude range (still the SNe with $z_{\text{SN}} < 0.05$ were excluded as irrelevant for our analysis). The lower panel of Fig.2 shows the $T_{\text{SN}}/z_{\text{SN}}$ diagram built for the whole SN sample, that includes also the SNe within the galactic plane region. As expected for this data, the significance of the $T_{\text{SN}}/z_{\text{SN}}$ correlation is reduced, with the Pearson correlation coefficient being $r = 0.23 \pm 0.10$ (as before, the confidence interval for this coefficient was calculated by bootstrapping the correlation).

Nevertheless, the noisy effect of the local galactic foreground on the $T_{\text{SN}}/z_{\text{SN}}$ correlation is not very big: the average \overline{T}_{SN} values calculated for three large redshift bins still indicate a 6.6σ -anomaly for the redshift range $0.3 < z_2 < 0.8$. These \overline{T}_{SN} values for the whole sample, as well as their standard errors, signal-to-noise ratios and SN sample sizes, are given in Table 2. By comparing Tables 1 and 2 we can conclude that the local galactic foreground might obscure the systematic contribution from the distant foreground by about 30%. In order to facilitate further checks of the found

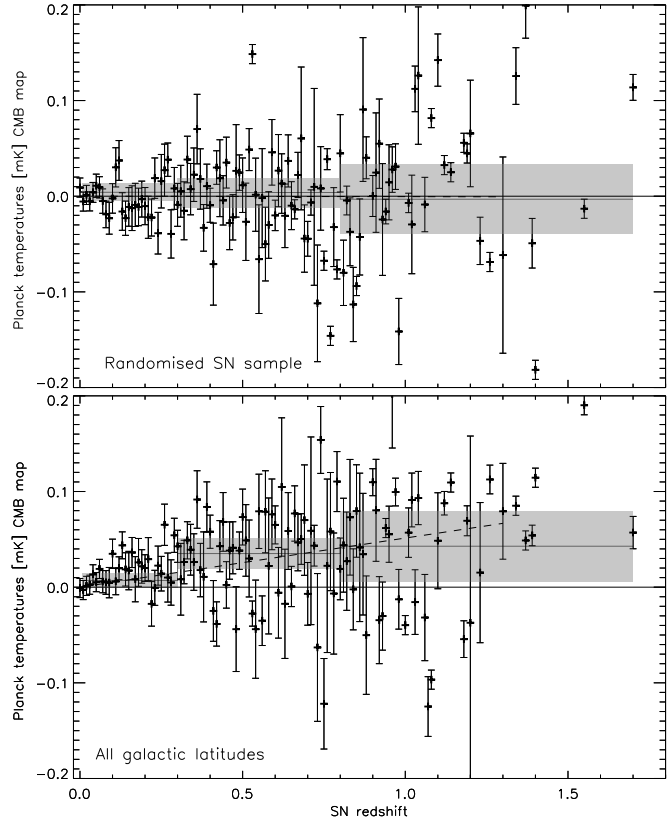


Figure 2. Upper panel: the $T_{\text{SN}}/z_{\text{SN}}$ diagram for the randomised SN sample does not show any temperature anomalies; lower panel: the $T_{\text{SN}}/z_{\text{SN}}$ diagram for the whole SN sample including the SNe within the galactic plane shows a small but still statistically significant anomaly for the redshifts $0.3 < z_2 < 0.8$. The shaded areas indicate the 3σ -tolerances around the \overline{T}_{SN} averaged for three SN redshift intervals: $z_1 < 0.3$, $0.3 < z_2 < 0.8$ and $z_3 > 0.8$.

Table 2. Temperatures $\overline{T}_{\text{SN}}^{\text{gal}}$ averaged for three large redshift intervals (bins) $0.0 < z_1 < 0.3$, $0.3 < z_2 < 0.8$ and $0.8 < z_3 < 1.7$ for the whole SN sample, including the SNe near the galactic plane (see Fig.2 lower panel).

Characteristics	z_1	z_2	z_3
$\overline{T}_{\text{SN}}^{\text{gal}}$ [μK]	+7.0	+35.1	+42.8
$\sigma_{\overline{T}_{\text{SN}}^{\text{gal}}}$ [μK]	± 2.4	± 5.3	± 12.3
Signal-to-noise ratio [σ]	2.8	6.6	3.5
Sample size	4601	608	109

anomaly by the other researches, we have generated the full catalogue of SNe with the associated Planck CMB map temperatures at the SN locations, which we have provided in the form of an Appendix to this paper (an ASCII table available online). A small extract of this catalogue is presented in Table 3 as an example showing the first three and the last three entries. This catalogue includes 6359 SN entries arranged in the ascending SN redshift order (6 entries were excluded as they were lacking the SN sky coordinates). The columns of this table provide the source number N, the source name (SN name), right ascension R.A. (in hours minutes and sec-

Table 3. Catalogue of supernovae stars with the associated Planck CMB map pixel temperatures at the SN locations (this table shows only the first and the last three entries of the catalogue, whereas the full catalogue is available online in the form of an ASCII table).

N	SN name	R. A. <i>h m s</i>	Decl. ° ' "	<i>z</i>	T_{CMB} [mK]	T_{err} [mK]	<i>l</i> [deg]	<i>b</i> [deg]	Galaxy name	Galaxy type	Mask	SN type
0001	1885A	00 42 43.00	+41 16 04.0	0.000	-0.097	0.041	121.1698	-21.5741	NGC0224	Sb	0	IPec
0002	1938C	13 16 08.28	+25 09 40.0	0.000	0.122	0.023	14.7736	84.1190	-	-	0	-
0003	1950D	08 43 05.44	+18 09 48.0	0.000	-0.195	0.010	207.8540	32.5486	-	-	0	-
...
6357	2002fx	03 32 06.80	-27 44 34.4	1.400	0.114	0.009	223.4417	-54.5049	-	-	0	Ia
6358	2003ak	03 32 46.90	-27 54 49.3	1.551	0.190	0.005	223.7699	-54.3841	-	-	0	Ia
6359	1997ff	12 36 44.38	+62 12 41.9	1.700	0.057	0.017	125.9055	54.8317	-	-	0	-

onds), and declination Decl. (in degrees, arcminutes and arcseconds) of the source, its redshift z , Planck CMB map pixel temperature at the SN location T_{CMB} and its variance T_{err} (both in mK), the SN galactic longitude l and latitude b (both in degrees), the name and type of the SN host galaxy (if available), the value of the combined galactic plane and point source mask and the SN type (if available).

3 DISTINCTION BETWEEN DIFFERENT SUPERNOVA TYPES

As we have mentioned, one of our interpretations of the revealed anomaly was that it might be due to some possible contribution of thermal emission from dust residing in the SN host galaxies. For checking this possibility, we have split our SN sample into two subsamples, one containing only the SNe of type Ia (1937 sources for $|b| > 40^\circ$), and the other with the rest of the SNe (1411 sources for $|b| > 40^\circ$, mostly of the types II, Ib and Ic). The SNe from the latter sample typically occur in galaxies with higher star formation rates, while SNe Ia can occur in any galaxy (Filippenko 1989; Farrah et al. 2002; Childress et al. 2013). What we expected was an enhancement of this correlation for the SNe in the galaxies with high star formation rates and containing large amounts of dust, that is, for the type II, Ib and Ic SNe.

However, contrary to what we expected, the significance of the correlation became higher for the Ia type SNe, with the correlation significance p -value being reduced from $2.9 \cdot 10^{-5}$ for the whole SNe sample to $7.3 \cdot 10^{-9}$ for the SN of the type Ia subsample, whereas for the rest of the SNe the p -value increased dramatically to $p = 0.812$ and the significance of the Pearson's correlation coefficient decreased to 0.9σ , revealing no correlation whatsoever for the other SN types. The results of our statistical tests for these two SN subsamples, as well as for the whole sample, are summarised in Table 4. The last entry in this Table gives the number of sources per sample in the selected latitude range. The first entry gives the slopes ξ of the regression lines characterising the relationship between T_{SN} and z_{SN} expressed in μK per unit redshift interval. The steepest of these slopes corresponds to the type Ia SNe. The confidence intervals for the Pearson's correlation coefficients (second line of the Table) were calculated by bootstrapping the correlation. The correlation significance p -value is given in the third line of this Table. The lowest p -value, which indicates the highest statistical significance of the correlation, also points at the

Table 4. Results of the correlation tests for three SN samples.

Characteristics	All SNe	SN Ia	The rest of SNe
ξ [μK]	58.0 ± 9.0	72.2 ± 10.9	20.7 ± 24.1
Pearson's r	0.38 ± 0.08	0.45 ± 0.09	-0.13 ± 0.14
p -value	$2.9 \cdot 10^{-5}$	$7.3 \cdot 10^{-9}$	0.812
$\overline{T}_{\text{SN}}^{(0.8,1.7)}$ [μK]	$+63.4 \pm 12.9$	76.6 ± 11.8	-36.9 ± 34.9
Sample size	3348	1937	1411

type Ia SNe as the objects likely to be responsible for the correlation. Therefore, our next statistical test (Section 4) was made by using only the sample of the type Ia SNe.

4 CORRELATION TESTS FOR DIFFERENT PLANCK FREQUENCY BANDS

When analysing the anomaly in the WMAP data, we have checked (and rejected) the possibility of this anomaly being caused by the Sunyaev-Zeldovich effect. There were only small, statistically insignificant, variations in the slopes of the regression lines $T_{\text{SN}}/z_{\text{SN}}$ obtained for three WMAP frequency bands, 40, 60 and 90 GHz. In fact, it was difficult to expect detecting the SZ effect by using the WMAP data because in order to see this effect clearly one has to use frequency bands below and above the so-called cross-over frequency 218 GHz, whereas all three WMAP bands which we used for this check had frequencies below 218 GHz.

The HFI and Low Frequency Instrument (LFI) onboard the Planck satellite provided a much wider frequency coverage by Planck's nine frequency bands ranging from 30 to 857 GHz. Although the Planck legacy archive contains just one CMB map generated by combining the measurements made in the HFI frequency bands, these bands contain information about the foreground emission which is a mixture of the local and remote foreground emissions, with a larger contribution from the local foreground at low galactic latitudes and lower frequencies. Actually, combinations of different frequency bands were used by the Planck team for producing the Planck foreground emission maps. We can use both the frequency band maps and foreground emission maps for our correlation analysis, provided that we apply the Planck point source and galactic plane masks and exclude the galactic latitudes $|b| < 40^\circ$ from the consideration to reduce the noisy effect from the local foreground.

When building the diagrams for different frequency

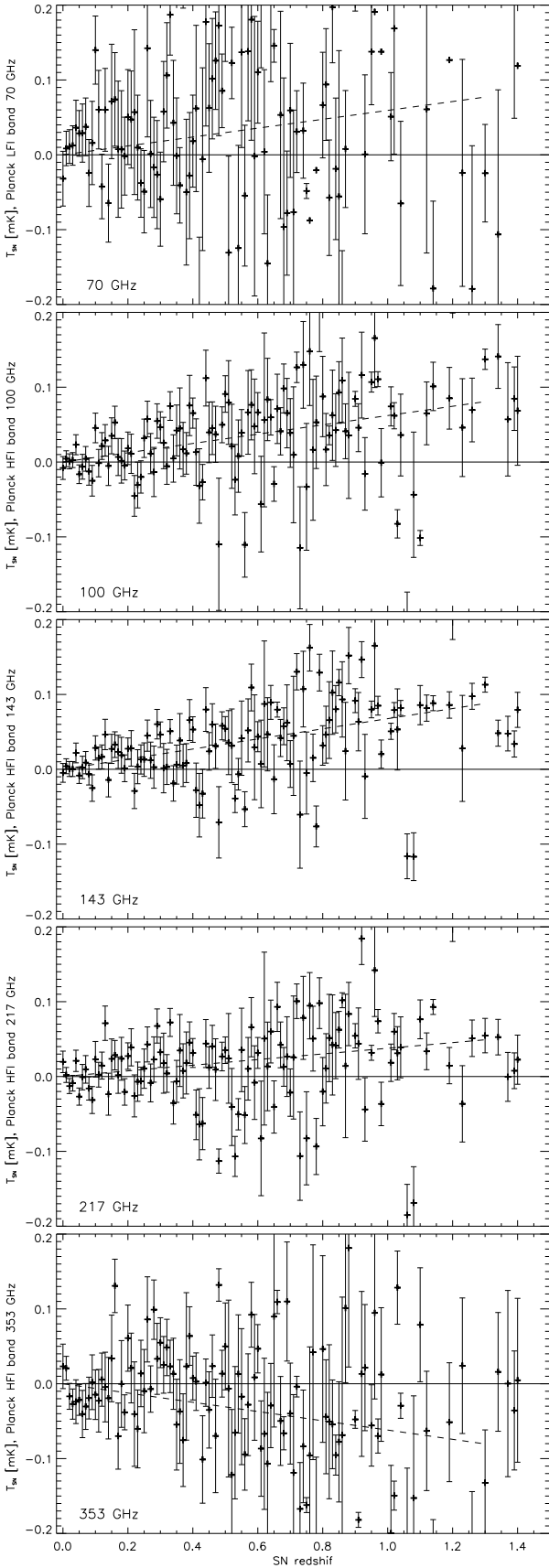


Figure 3. $T_{\text{SN}}/z_{\text{SN}}$ diagrams constructed for five Planck frequency bands: LFI 70 GHz, HFI 100, 143, 217 and 353 GHz.

Table 5. Slopes of the regression lines characterising the relationship between T_{SN} and z_{SN} for five Planck frequency bands, two foreground component maps (the low-frequency foreground map LFF, thermal dust foreground, TDF) and for the CMB lensing potential map CLPM.

Planck band	Slope ξ_ν [μK]	Pearson's r	Significance [σ]
70 GHz	59.3 ± 36.4	0.12 ± 0.09	1.3
100 GHz	62.1 ± 13.6	0.35 ± 0.11	3.1
143 GHz	67.6 ± 6.3	0.43 ± 0.08	5.4
217 GHz	37.7 ± 8.4	0.21 ± 0.09	2.3
353 GHz	-61.8 ± 18.2	-0.27 ± 0.09	3.0
LFF 30 GHz	-52.7 ± 15.0	-0.26 ± 0.12	2.2
TDF 353 GHz	-73.1 ± 29.0	-0.34 ± 0.08	4.2
CLPM	-55.5 ± 61.1	-0.12 ± 0.11	1.1

bands, we have found that the scatter of the binned temperatures T_{SN} was extremely large for the bands 30, 44, 545 and 857 GHz, so we have used only the remaining five Planck frequency bands 70, 100, 143, 217 and 353 GHz for which the scatter of the data points was tolerable (these diagrams are shown in Fig.3). The results of our correlation tests applied to these five diagrams are presented in Table 5.

The lowest significance of the correlation was obtained for the Planck LFI 70 GHz frequency band. For this band $r = 0.12 \pm 0.09$, which means that the null-hypothesis about the absence of any correlation in this case cannot be rejected. However, the slopes of the regression lines $T_{\text{SN}}/z_{\text{SN}}$ for the Planck bands 70 and 100 GHz, $\xi = +59.3 \pm 36.4 \mu\text{K}$ and $\xi = +62.1 \pm 13.6 \mu\text{K}$, match, within the 3σ tolerance intervals, the slopes corresponding to the WMAP bands of 61 and 94 GHz, $\xi = +36.6 \pm 7.6 \mu\text{K}$ and $\xi = +32.2 \pm 7.8 \mu\text{K}$, respectively, which were obtained in our previous work (Yershov et al. 2012). In the Planck case the low significance of these coefficients is due to the fact that they were calculated by using frequency maps containing emission from local foreground, whereas in the WMAP case it was possible to use cleaned CMB maps. The highest significance of the correlation is obtained for the HFI 143 GHz frequency band with the significance level of 5.1σ for the correlation coefficient.

The Sunyaev-Zeldovich effect should cause a decrease in the CMB intensity at the frequencies below 218 GHz and an increase at higher frequencies. Therefore, if the observed anomaly were caused by this effect, we would expect a higher positive anomaly in our plots for the 353 GHz band. However, the effect we see for this band in Fig.3 (lower panel) is the opposite: the anomaly in the 353 GHz band is negative, and the slope of the regression line for this band is negative as well, $\xi_{353} = -61.8 \pm 18.2 \mu\text{K}$. Thus, we can confidently exclude the SZ effect as the possible cause of the discussed anomaly.

The remaining possibility is either the ISW effect caused by the gravitational potential wells of the galaxy clusters hosting the SNe or some contaminating emission from dust and/or gas residing in the vicinity of the SN host galaxies. The observed frequency dependence of T_{SN} from z_{SN} and the fact that the strongest correlation corresponds to the Planck frequency channel of 143 GHz suggest that the spectral energy distribution of the anomalous emission is similar

to that of the CMB. This supports the idea of the ISW effect behind the seen correlation. Alternatively, if this anomaly is related to the emission from intergalactic matter distributed across large volumes at distances corresponding to $z > 0.3$, then this matter must be thermalised.

Among the Planck products, there are two foreground distribution maps derived by the Planck team by using the data from different frequency channels: the Low-Frequency Foreground (LFF) and the Thermal Dust Foreground (TDF) component maps. We have checked these maps for the presence of the discussed correlation. The calculated slopes of the regression lines $T_{\text{SN}}/z_{\text{SN}}$ and the corresponding Pearson's correlation coefficients for these two foreground maps are given in 6th and 7th entries of Table 5. The LFF map (normalised to the 30 GHz channel) does not show any significant correlation, whereas the TDF map (normalised to 353 GHz) reveals a negative correlation similar to that of the Planck 353 GHz frequency channel but with higher significance of about 4.2σ . Since this map can contain contributions from both local and remote dust, the negative slope of the $T_{\text{SN}}/z_{\text{SN}}$ correlation favours the remote black-body emission being responsible for this correlation.

The last entry of Table 5 gives the results of our correlation analysis of the Planck CMB Lensing Potential Map (CLPM) which reflects the distribution of gravitational potential wells leading to the ISW effect (since the CLPM data are dimensionless, we have scaled them to achieve a slope amplitude similar to those of the other entries of Table 5). The very low significance of the correlation between the CLPM amplitudes and z_{SN} casts the ISW effect to be a less favourable candidate to the mechanism responsible for the discussed $T_{\text{SN}}/z_{\text{SN}}$ correlation.

5 CONCLUSIONS

By using the recently released Planck satellite data we have not only confirmed the existence of the CMB anomaly previously reported for the WMAP data, but we have also found that the statistical significance of the correlation between the SNe redshifts and the temperature fluctuations of the CMB at the SNe locations is quite high. This significance becomes higher if, for our correlation analysis, we use a subsample of SNe of only the type Ia.

We have also shown that the found effect is frequency-dependent, with this dependence being opposite to the SZ effect. In our view, this correlation is likely to be related to either the integrated Sachs-Wolfe effect, some remote foreground emission from dust and/or gas, or to a combination of both effects.

If this anomaly is related to the clumps of matter (remote galaxies or galaxy clusters) traced by the presence of SNe then it might explain the findings of other authors showing a positive correlation between CMB and overdensities of galaxies – see, e.g., Ho et al. (2008). The possible impact of dusty galaxy clusters on the estimates of the cosmological parameter was also discussed by Serra et al. (2008), Dunkley et al. (2011) and Millea et al. (2012).

The observed systematic relationship between the SN redshifts and CMB temperature fluctuations should be further examined with the purpose to use it for reducing the contamination of CMB maps by distant foreground at

$z > 0.5$ and, thus, to increase the accuracy of determining the cosmological parameters.

ACKNOWLEDGEMENTS

The research has made use of the following archives: the Planck Legacy Archive operated by ESA's space astronomy centre; the Hierarchical Equal Area iso-Latitude Pixelisation (HEALPIX) software packages maintained by the Jet Propulsion Laboratory, California Institute of Technology, Pasadena; and the Supernovae Catalogue maintained by Sternberg Astronomical Institute, Moscow State University. The authors are grateful to the anonymous Referee whose very useful suggestions resulted in the essential improvements of this paper.

REFERENCES

- Bartunov O. S., Tsvetkov D. Yu., Pavlyuk N. N., 2007, *Highlights in Astr.*, 14, 316
 Childress M., Aldering G., Antilogus P., et al., 2013, *ApJ*, 770, 107
 Di Paola A., Larionov V., Arkharov A., et al., 2002, *A&A*, 393, L21
 Dunkley J., et al., 2011, *ApJ*, 739, 52
 Efron B., 1979, *Ann. Statist.*, 7, 1
 Elias-Rosa N., Benetti S., Turatto M., et al., 2008, *MNRAS*, 384, 107
 Farrah D., Meikle W. P. S., Clements D., et al., 2002, *MNRAS*, 336, L17
 Filippenko A. V., 1989, *Publ. Astr. Soc. Pacific*, 101, 588
 Gorski K. M., Hivon E., Banday A. J., et al., 2005, *ApJ*, 622, 759
 Goto T., Szapudi I., Granett B. R., 2012, *MNRAS*, 422, L77
 Ho S., Hirata C. M., Padmanabhan N., et al., 2008, *Phys. Rev. D*, 78, 043518
 Kozlovski S., Kochanek C. S., Stern D., et al., 2010, *ApJ*, 722, 1624
 Mattila S., Dahlen T., Efstathiou A., et al., 2012, *ApJ*, 756, 111
 Millea M., Doré O., Dudley J., et al., 2012, *ApJ*, 746, 4
 Planck Collaboration, 2014, *A&A*, in press, doi: 10.1051/0004-6361/201321529, arXiv:1303.5062[astro-ph.CO]
 Romero-Canizales C., Matilla S., Alberdi A., et al., 2011, *MNRAS*, 415, 2688
 Sachs R. K., Wolfe A. M. 1967, *ApJ*, 147, 73
 Serra P., Cooray A., Amblard A., 2008, *Phys. Rev. D* 78, 043004
 Sunyaev R. A., Zeldovich Ya. B., 1970, *Astrophys. Space Sci.*, 7, 3
 Vink J., 2004, *ApJ*, 604, 693
 Yershov V. N., Orlov V. V., Raikov A. A., 2012, *MNRAS*, 423, 2147

SUPPORTING INFORMATION

Additional Supporting Information may be found in the online version of this article:

Table 3

<http://mnras.oxfordjournals.org/lookup/suppl/doi:10.1093/mnras/st>